Numerical Analysis of Nematic Liquid Crystals as Applied to Tunable Antennas

N.C. Papanicolaou[1] M.A. Christou[1] A.C. Polycarpou[2]

[1]Department of Mathematics, University of Nicosia

[2]Department of Electrical and Computer Engineering, University of Nicosia

6th AMiTaNS, Albena, Bulgaria, June 26 - July 1, 2014

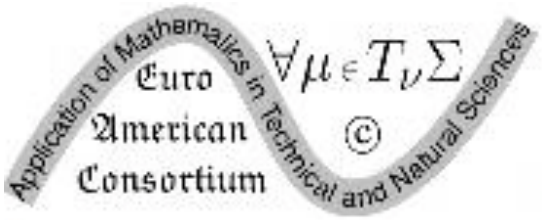

Outline

History of Liquid Crystals

- In *1888*, Austrian botanist and chemist Friedrich Reinitzer (1857-1927), whilst experimenting with cholesteryl benzoate, observed striking color effects and discovered that it exhibited a double melting point: At 145.5°C it melts into a cloudy liquid, and at 178.5°C it melts again and the cloudy liquid becomes clear.

- He collaborated with the German crystallographer Otto Lehmann (1855-1922), who examined the intermediate cloudy fluid, and reported seeing crystallites. Lehmann devised the name "liquid crystals" in his *1904* work "Flüssige Kristalle".

Thermotropic

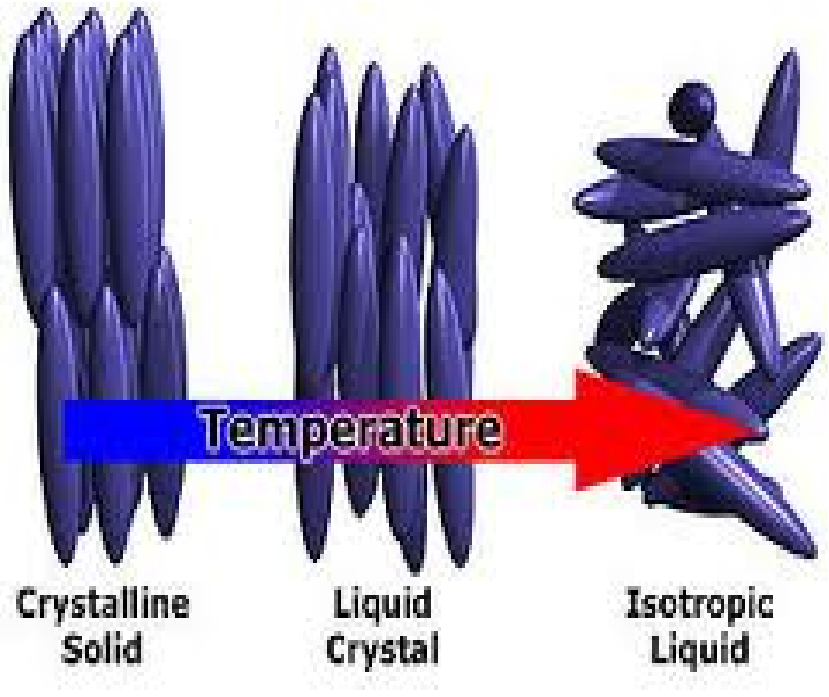

Figure : Dependence of liquid crystal materials on temperature.

Brilliant Colors

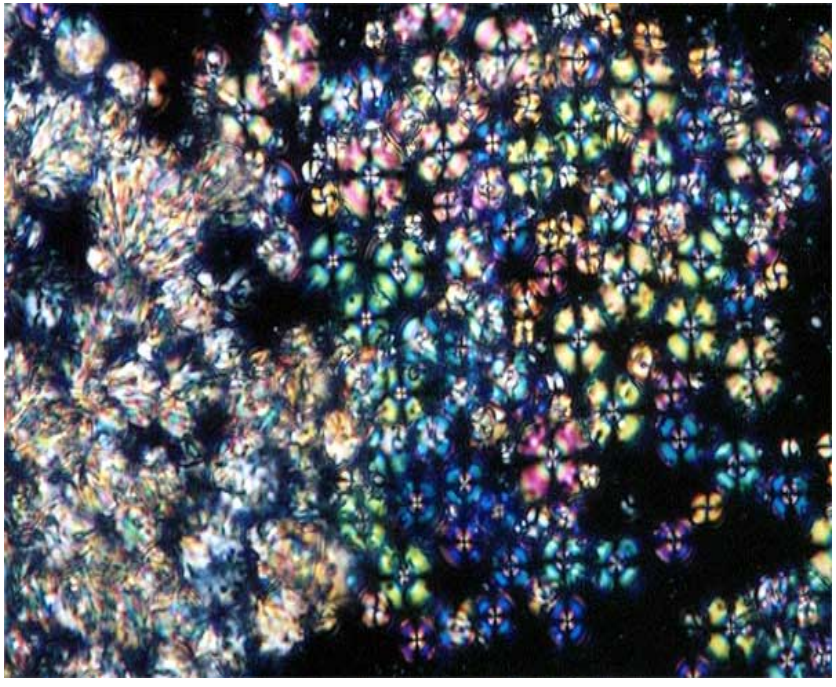

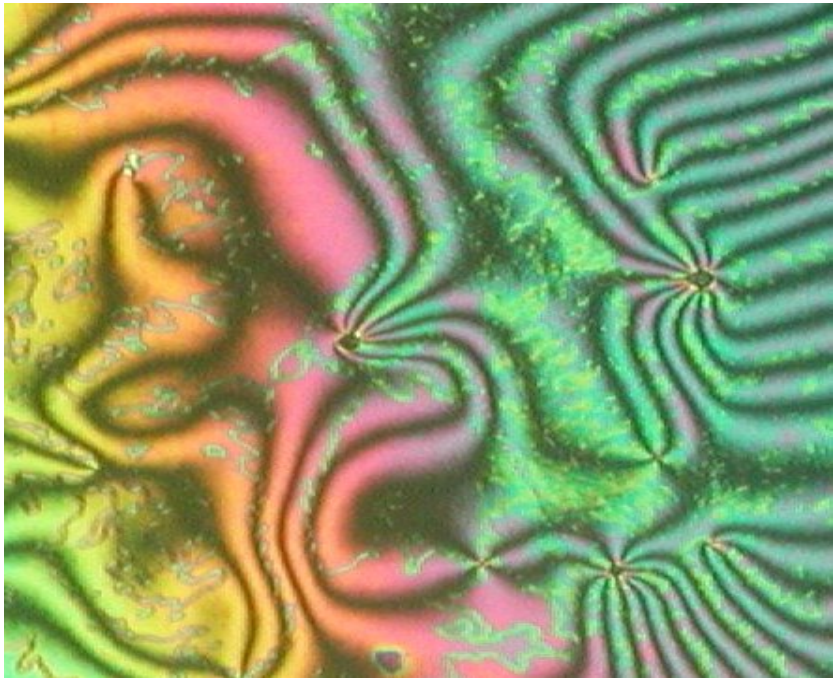

Figure : Images of liquid crystals using optical microscopy and polarized light.

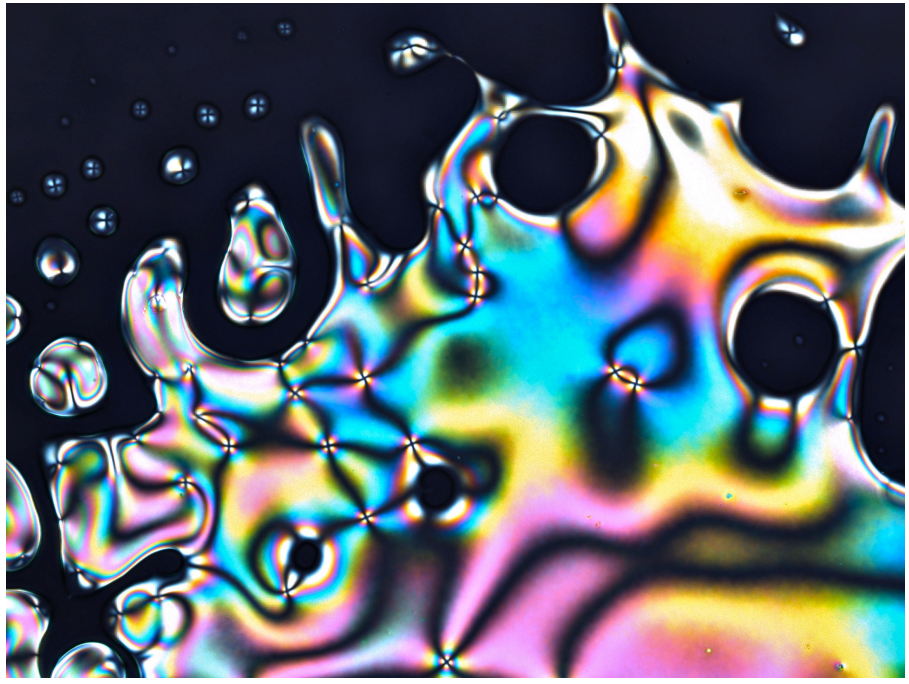

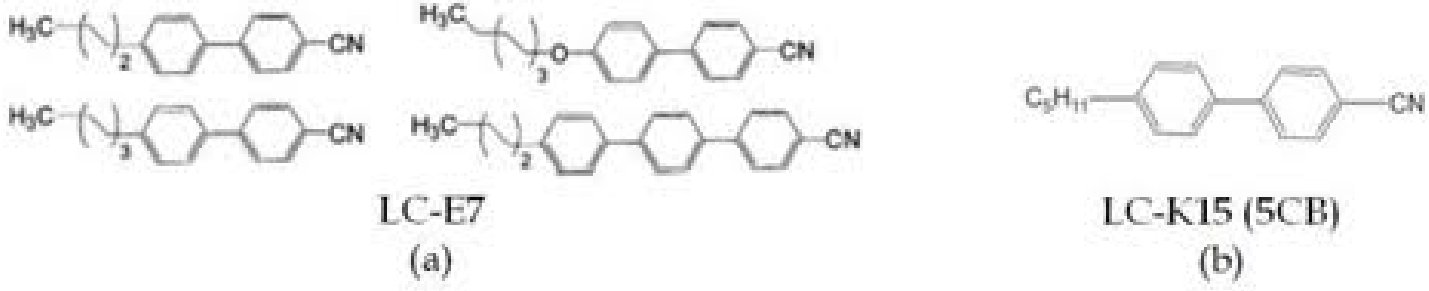

Figure : Top: 5CB using optical microscopy and polarized light. Bottom: Chemical formulas of E7 and 5CB type LCs.

Applications of Liquid Crystals

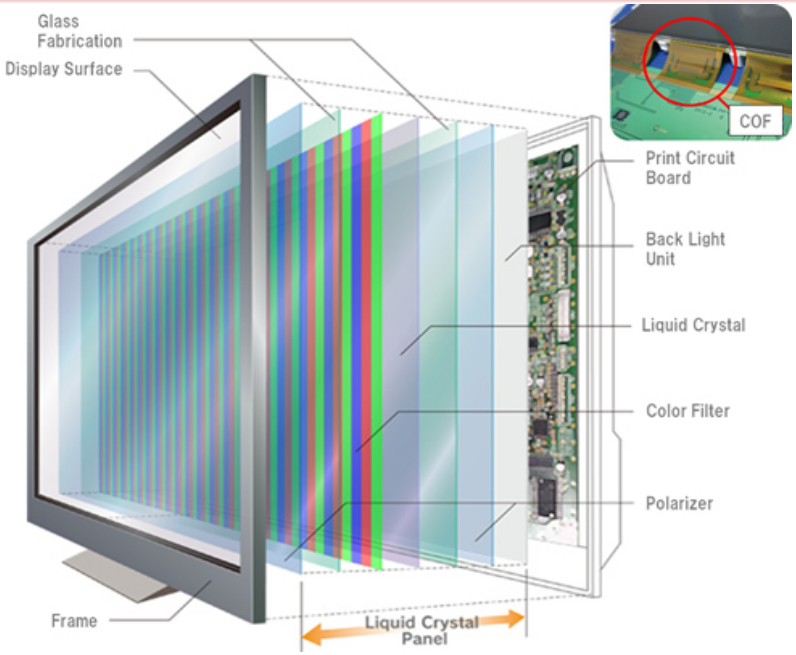

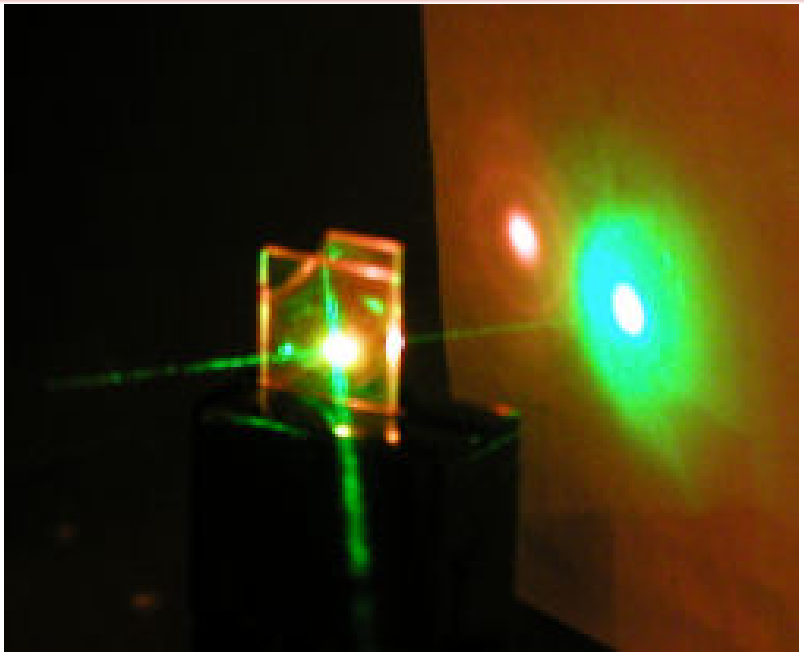

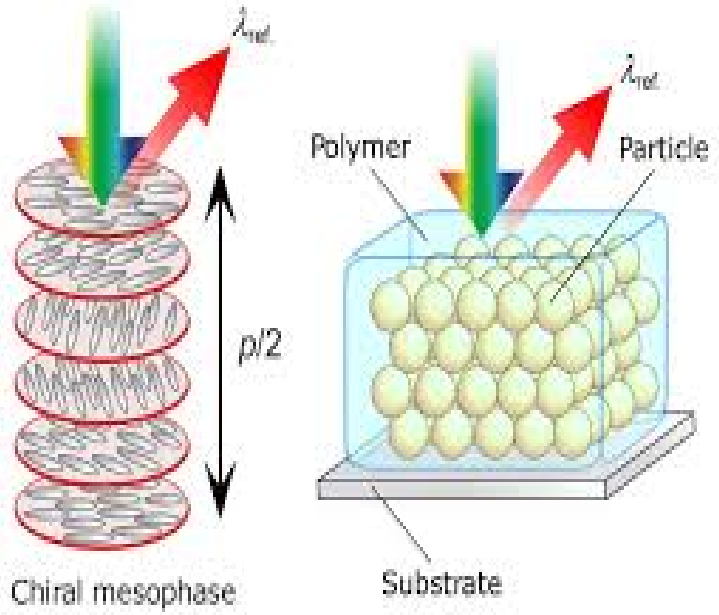

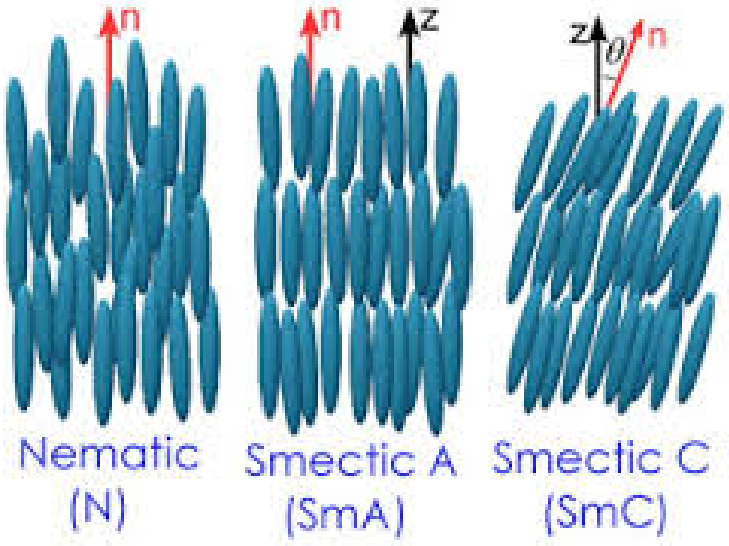

- The versatility of LCs is due to their electro-optical properties (anisotropic, birefringent and tunable).
- Nematic liquid crystals owe their properties to their molecular structure. Their molecules are rod-like (calametic) and in this mesophase they macroscopically point in a preferred direction called the *director*.
- The orientation of the directors determines the electrical properties of the liquid crystal. Thus, the relative dielectric tensor of the LC is a function of the director angle.

Patch Antenna with NLC Substrate

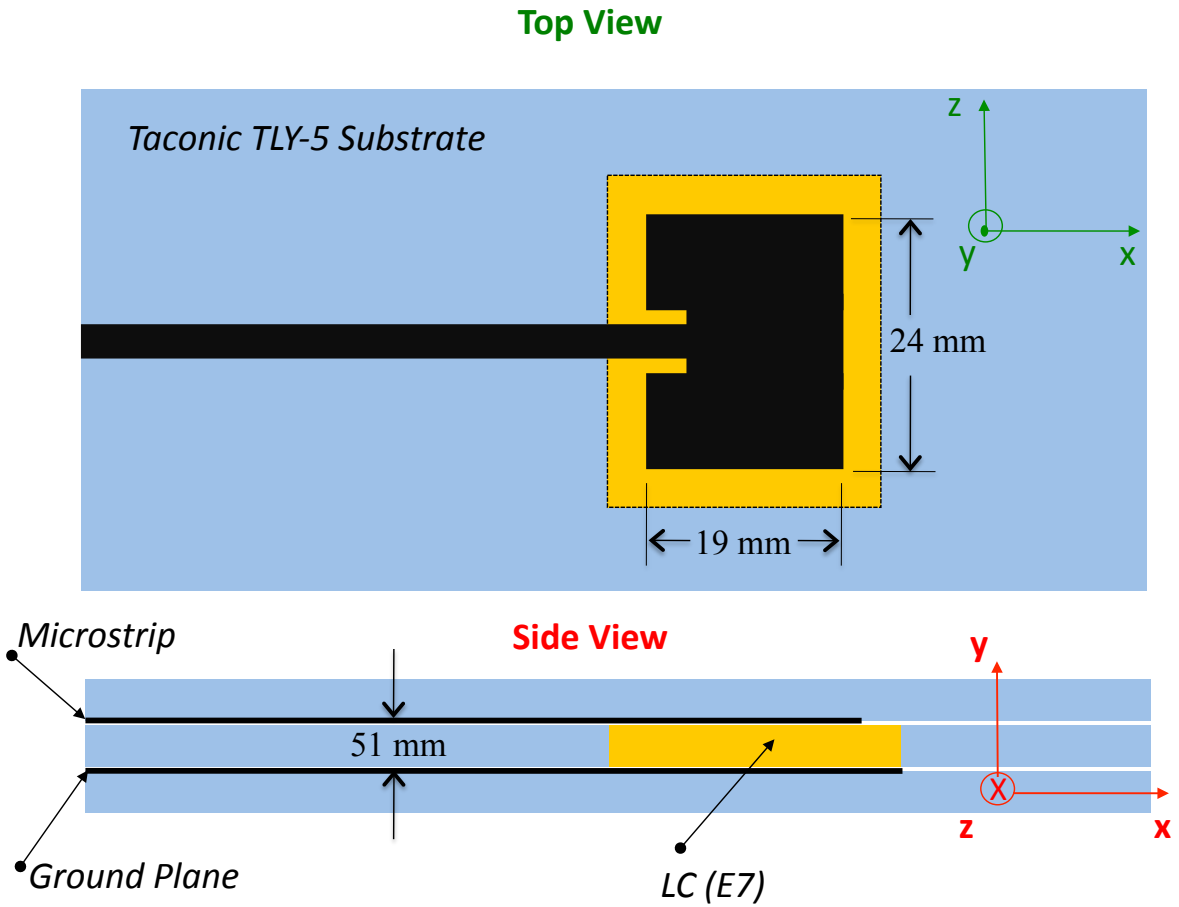

Figure : Patch antenna design *(Liu and Langley, Electronics Letters, 2008)*

- Modern wireless communications systems require use of multiple antennas residing on small platforms (e.g. tablets, smartphones). Reducing the antenna count saves valuable space for additional functionalities and features. This can be achieved by using *frequency-agile* antennas.

- Very little work has been done on the design, modeling, and testing of LC-based patch antennas. Previous works used effective values in their models ignoring the LC material anisotropy *(Liu and Langley 2008)* whereas others also did not consider losses *(Martin et al. 2003, Bose and Sinha 2008)*.

- Here, the geometry proposed by Liu and Langley is used to test the accuracy of our model. Our method consists of:

  I. *Accurately solving for the director field inside the liquid crystal* under certain biasing conditions. The obtained values are used to obtain the LC's permittivity and loss tangent tensors.

  II. Using the tensors as input, the *radiation characteristics of the LC-based patch antenna are obtained*.

Part I: Characterizing the LC layer

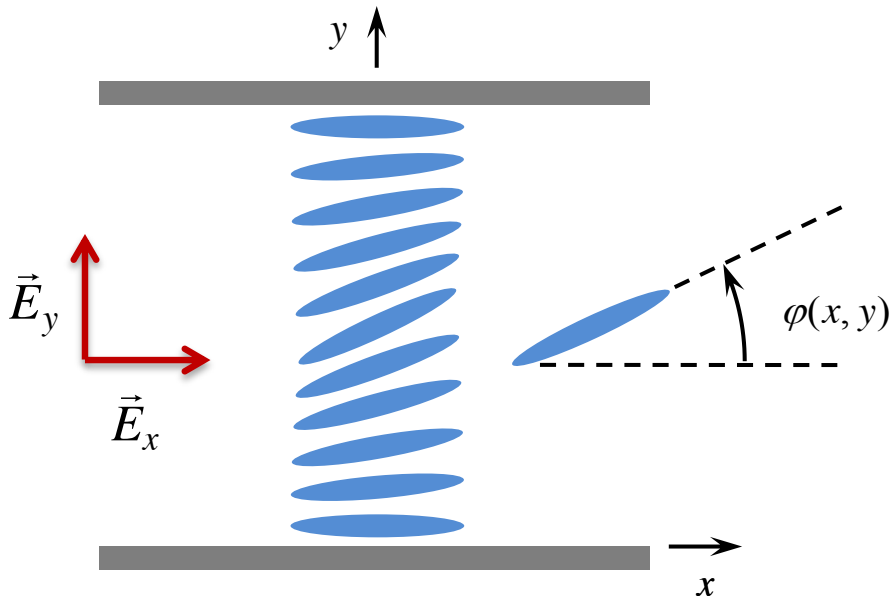

- An external DC (low-frequency AC) electric field is applied to the NLC-cell. This *excites* the LC, changing the orientation angle of the directors.
- This alters the dielectric tensor and hence affects the intensity of the electric field inside the cell. In turn, the field intensity leads to corresponding new values for the director field.
- This a coupled problem. The (quasi-static) Poisson equation in a charge-free region which governs the electric field inside the LC is intrinsically linked to the nonlinear PDE for the director field.

Non-Linear PDE for the Director Field

- Assuming z-invariance and no twist, the director orientation is defined by the unit vector in the $xy-$plane $\hat{n} = (\cos\phi, \sin\phi, 0)$, where $\phi = \phi(x, y)$ is the director tilt angle.

- The response of the directors in the presence of an electric field is governed by the Oseen-Frank free energy functional

$$\mathfrak{F} = \frac{1}{2}\int \Big[k_{11}(\nabla\cdot\hat{n})^2 + k_{22}[\hat{n}\cdot(\nabla\times\hat{n})]^2 + k_{33}|\hat{n}\times(\nabla\times\hat{n})|^2 - \epsilon_0\Big[\Delta\epsilon(\hat{n}\cdot\vec{E})^2 + \epsilon_\perp|\vec{E}|^2\Big]\Big]\, d^3r \tag{1}$$

k_{11}, k_{22}, and k_{33}	:	splay, twist and bend elastic constants
$\vec{E} = (E_x, E_y, E_z)$	:	electric field
ϵ_0	:	electric permittivity of free space
$\Delta\epsilon = \epsilon_{\parallel} - \epsilon_\perp$	:	birefringence
$\epsilon_{\parallel}$	:	relative permittivity of crystal in direction parallel to director
$\epsilon_\perp$	:	relative permittivity of crystal in direction perpendicular to director

- Functional $\mathfrak{F}$ in Eq. (1) can be minimized using the Euler-Lagrange equation

$$\frac{\partial f}{\partial \phi} - \frac{\partial}{\partial x}\frac{\partial f}{\partial \phi_x} - \frac{\partial}{\partial y}\frac{\partial f}{\partial \phi_y} = 0\,, \tag{2}$$

where

$$\begin{aligned} f = \frac{1}{2}\big[& k_{11}(\cos\phi\phi_y - \sin\phi\phi_x)^2 + k_{33}(\cos\phi\phi_x + \sin\phi\phi_y)^2 \\ & - \epsilon_0[\Delta\epsilon(\cos\phi E_x + \sin\phi E_y)^2 + \epsilon_\perp(E_x^2 + E_y^2 + E_z^2)]\,\big]\,. \end{aligned} \tag{3}$$

- Substituting (3) into (2), and manipulating yields the *Nonlinear PDE for the director field*

$$\begin{aligned} & 2(k_{11}\sin^2\phi + k_{33}\cos^2\phi)\frac{\partial^2\phi}{\partial x^2} + 2(k_{11}\cos^2\phi + k_{33}\sin^2\phi)\frac{\partial^2\phi}{\partial y^2} \\ & -(k_{11}-k_{33})\sin 2\phi\left[\left(\frac{\partial\phi}{\partial x}\right)^2 - \left(\frac{\partial\phi}{\partial y}\right)^2\right] - 2(k_{11}-k_{33})\left[\sin 2\phi\frac{\partial^2\phi}{\partial x\partial y} + \cos 2\phi\frac{\partial\phi}{\partial x}\frac{\partial\phi}{\partial y}\right] \\ & + \epsilon_0\Delta\epsilon[\sin 2\phi(E_y^2 - E_x^2) + 2\cos 2\phi E_x E_y] = 0. \end{aligned} \tag{4}$$

Strong anchoring: Dirichlet BC's.

$$\phi(x,y) = \phi_0\ (= 2^\circ) \text{ at } y = 0, d. \tag{5}$$

The Potential Equation

The DC/low-frequency AC electric field in the structure is governed by *Poisson's quasistatic equation* in a charge-free region:

$$\nabla \cdot (\hat{\epsilon} \nabla V) = 0, \tag{6}$$

where $\hat{\epsilon}$ is the *relative permittivity tensor* of the non-homogeneous LC medium given by

$$\hat{\epsilon}(x,y) = \begin{bmatrix} \epsilon_{xx}(x,y) & \epsilon_{xy}(x,y) & 0 \\ \epsilon_{yx}(x,y) & \epsilon_{yy}(x,y) & 0 \\ 0 & 0 & \epsilon_{zz}(x,y) \end{bmatrix}, \tag{7a}$$

with components

$$\begin{aligned} \epsilon_{xx} &= \epsilon_{\perp} + \Delta\epsilon \cos^2 \phi(x,y), \\ \epsilon_{xy} &= \epsilon_{yx} = \Delta\epsilon \sin \phi(x,y) \cos \phi(x,y), \\ \epsilon_{yy} &= \epsilon_{\perp} + \Delta\epsilon \sin^2 \phi(x,y), \\ \epsilon_{zz} &= \epsilon_{\perp}. \end{aligned} \tag{7b}$$

- Utilizing (6, 7) and assuming z-invariance, *we obtain the equation governing the electric potential inside the LC*

$$\epsilon_{xx}\frac{\partial^2 V}{\partial x^2}+\epsilon_{yy}\frac{\partial^2 V}{\partial y^2}+2\epsilon_{xy}\frac{\partial^2 V}{\partial x\partial y} + \left(\frac{\partial \epsilon_{xx}}{\partial x}+\frac{\partial \epsilon_{xy}}{\partial y}\right)\frac{\partial V}{\partial x}+\left(\frac{\partial \epsilon_{xy}}{\partial x}+\frac{\partial \epsilon_{yy}}{\partial y}\right)\frac{\partial V}{\partial y}=0. \tag{8}$$

$$\left.\frac{\partial V}{\partial x}\right|_{x=x_L}=\left.\frac{\partial V}{\partial x}\right|_{x=x_R}=0\ , \tag{9a}$$

$$V(x,y=d)=V_0 \quad \text{for} \quad x\in[x_{L_1},x_{R_1}]\cup[x_{L_2},x_{R_2}]\ , \tag{9b}$$

$$V(x,y=0)=0 \quad \forall x\in[x_L,x_R]\ , \tag{9c}$$

- The electric field at a point in the crystal is computed by taking the gradient of the electric potential

$$\vec{E}=-\nabla V \tag{10}$$

- *The coupled system of equations (4, 8) is to be solved iteratively until convergence is reached.*

Algorithm Outline

For each applied voltage value V_0:

1. Initial values are assumed for the director field.
2. The relative permittivities are evaluated and then the equation (8) for the electric potential is solved.
3. Once the electric potential is obtained, the electric field is calculated by taking the gradient of V. Knowing the governing field distribution, equation (4) is solved to obtain the tilt angle of the directors throughout the crystal.
4. Steps 2-3 are repeated until convergence is reached.
5. Once the director field is known throughout the LC, the average value is calculated. This is used to compute the relative permittivity tensor and the loss tangents.

Finite Difference Schemes

Eqn (4) is discretized by utilizing FD approximations.

(a) Three-point Explicit Scheme:

$$\phi_{i,j}^{n+1} = \left(\frac{1}{\omega + \hat{C}_8}\right)\left[\omega\phi_{i,j}^{n} + \sum_{i=1}^{7}\hat{C}_i\right] \tag{11}$$

where

$$\begin{aligned}
&\hat{C}_1 = C_1(\phi_{i+1,j}^n + \phi_{i-1,j}^n) && , \quad \hat{C}_2 = C_2(\phi_{i,j+1}^n + \phi_{i,j-1}^n),\\
&\hat{C}_3 = C_3(\phi_{i+1,j+1}^n - \phi_{i+1,j-1}^n - \phi_{i-1,j+1}^n + \phi_{i-1,j-1}^n) && ,\\
&\hat{C}_4 = C_4(\phi_{i+1,j}^n - \phi_{i-1,j}^n)(\phi_{i,j+1}^n + \phi_{i,j-1}^n) && ,\\
&\hat{C}_5 = C_5(\phi_{i,j+1}^n - \phi_{i,j-1}^n)^2 && , \quad \hat{C}_6 = C_6(\phi_{i+1,j}^n - \phi_{i-1,j}^n)^2,\\
&\hat{C}_7 = C_7 && , \quad \hat{C}_8 = 2(C_1 + C_2)\ ,
\end{aligned}$$

and

$$\begin{aligned}
&C_1 = 2(k_{11}\sin^2\phi_{i,j}^n + k_{33}\cos^2\phi_{i,j}^n)/D_x^2 && , C_2 = 2(k_{11}\cos^2\phi_{i,j}^n + k_{33}\sin^2\phi_{i,j}^n)/D_y^2,\\
&C_3 = (k_{33} - k_{11})\sin 2\phi_{i,j}^n/2D_xD_y && , C_4 = (k_{33} - k_{11})\cos 2\phi_{i,j}^n/2D_xD_y,\\
&C_5 = (k_{33} - k_{11})\sin 2\phi_{i,j}^n/4D_y^2 && , C_6 = (k_{11} - k_{33})\sin 2\phi_{i,j}^n/4D_x^2,\\
&C_7 = \epsilon_0\Delta\epsilon[\sin 2\phi_{i,j}^n(E_y^2 - E_x^2) + 2\cos 2\phi_{i,j}^n E_xE_y] && .
\end{aligned}$$

The relaxation parameter ω was introduced in order to accelerate convergence.

Fourth-order finite differences were employed resulting in the five-point explicit scheme:

(b) Five-point Explicit Scheme:

$$\phi_{i,j}^{n+1} = \left(\frac{1}{\omega + \hat{C}_8}\right)\left[\omega\phi_{i,j}^{n} + \sum_{i=1}^{7}\hat{C}_i\right] \tag{12}$$

where

$$\hat{C}_1 = C_1\left(-\phi_{i+2,j}^{n} + 16\phi_{i+1,j}^{n} + 16\phi_{i-1,j}^{n} - \phi_{i-2,j}^{n}\right), \quad \hat{C}_2 = C_2\left(-\phi_{i,j+2}^{n} + 16\phi_{i,j+1}^{n} + 16\phi_{i,j-1}^{n} - \phi_{i,j-2}^{n}\right),$$

$$\hat{C}_3 = C_3\Big(\phi_{i+2,j+2}^{n} - 8\phi_{i+2,j+1}^{n} + 8\phi_{i+2,j-1}^{n} - \phi_{i+2,j-2}^{n} - 8\phi_{i+1,j+2}^{n} + 64\phi_{i+1,j+1}^{n} - 64\phi_{i+1,j-1}^{n} + 8\phi_{i+1,j-2}^{n}$$
$$+ 8\phi_{i-1,j+2}^{n} - 64\phi_{i-1,j+1}^{n} + 64\phi_{i-1,j-1}^{n} - 8\phi_{i-1,j-2}^{n} - \phi_{i-2,j+2}^{n} + 8\phi_{i-2,j+1}^{n} - 8\phi_{i-2,j-1}^{n} + \phi_{i-2,j-2}^{n}\Big),$$

$$\hat{C}_4 = C_4\left(-\phi_{i+2,j}^{n} + 8\phi_{i+1,j}^{n} - 8\phi_{i-1,j}^{n} + \phi_{i-2,j}^{n}\right)\cdot\left(-\phi_{i,j+2}^{n} + 8\phi_{i,j+1}^{n} - 8\phi_{i,j-1}^{n} + \phi_{i,j-2}^{n}\right),$$

$$\hat{C}_5 = C_5\left(-\phi_{i,j+2}^{n} + 8\phi_{i,j+1}^{n} - 8\phi_{i,j-1}^{n} + \phi_{i,j-2}^{n}\right)^2, \quad \hat{C}_6 = C_6\left(-\phi_{i+2,j}^{n} + 8\phi_{i+1,j}^{n} - 8\phi_{i-1,j}^{n} + \phi_{i-2,j}^{n}\right)^2,$$

$$\hat{C}_7 = C_7, \quad \hat{C}_8 = 30(C_1 + C_2),$$

and

$$C_1 = (k_{11}\sin^2\phi_{i,j}^{n} + k_{33}\cos^2\phi_{i,j}^{n})/(6D_x^2) \quad , \quad C_2 = (k_{11}\cos^2\phi_{i,j}^{n} + k_{33}\sin^2\phi_{i,j}^{n})/(6D_y^2),$$
$$C_3 = (k_{33} - k_{11})\sin 2\phi_{i,j}^{n}/(72D_xD_y) \quad , \quad C_4 = (k_{33} - k_{11})\cos 2\phi_{i,j}^{n}/(72D_xD_y),$$
$$C_5 = (k_{33} - k_{11})\sin 2\phi_{i,j}^{n}/(144D_y^2) \quad , \quad C_6 = (k_{11} - k_{33})\sin 2\phi_{i,j}^{n}/(144D_x^2),$$
$$C_7 = \epsilon_0\Delta\epsilon[\sin 2\phi_{i,j}^{n}(E_y^2 - E_x^2) + 2\cos 2\phi_{i,j}^{n}E_xE_y] \quad .$$

The implicit numerical scheme is more stable and robust compared to the two aforementioned explicit schemes. Disadvantage: A linear system of equations must be solved at every iteration.

(c) Three-point Implicit Scheme:

$$
\begin{aligned}
&C_1 \frac{\partial^2 \phi^{n+1}}{\partial x^2} + C_2 \frac{\partial^2 \phi^{n+1}}{\partial y^2} + C_3 \frac{\partial^2 \phi^{n+1}}{\partial x \partial y} \\
&+ C_4 \left[\omega_3 \frac{\partial \phi^{n+1}}{\partial x} \frac{\partial \phi^n}{\partial y} + \omega_3 \frac{\partial \phi^n}{\partial x} \frac{\partial \phi^{n+1}}{\partial y} + (1 - 2\omega_3) \frac{\partial \phi^n}{\partial x} \frac{\partial \phi^n}{\partial y} \right] \\
&+ C_5 \left[\omega_2 \frac{\partial \phi^{n+1}}{\partial y} \frac{\partial \phi^n}{\partial y} + (1 - \omega_2) \frac{\partial \phi^n}{\partial y} \frac{\partial \phi^n}{\partial y} \right] \\
&+ C_6 \left[\omega_1 \frac{\partial \phi^{n+1}}{\partial x} \frac{\partial \phi^n}{\partial x} + (1 - \omega_1) \frac{\partial \phi^n}{\partial x} \frac{\partial \phi^n}{\partial x} \right] + C_7 = 0 \,.
\end{aligned}
$$

where C_i's for $i = 1, \ldots, 7$ were defined earlier. The parameters ω_1, ω_2, and ω_3 take values between 0 and 1. The derivative terms are discretized and re-arranged.

Comparison/Remarks on Numerical Schemes

- The problem was solved for benchmark geometries that appeared in the literature. *All three FD schemes provided* ***identical results***.
- **Computational time:** The five-point scheme with relaxation provides faster results as compared to the three-point scheme.
- **Stability:** The relaxation parameter plays an important role in the stability (and convergence speed) of both explicit schemes.
- The **implicit scheme** provides a robust method for the solution of the underlined problem. However, the implementation of the method requires solution of a matrix system per iteration which is computationally expensive.

Discretization of Poisson's equation

A similar approach is followed in the discretization of Poissson's equation. The second-order discretized equation inside the crystal is

$$
\begin{aligned}
V_{ij}^{k+1} = & \left\{ \epsilon_{ij}^{xx} \frac{V_{i+1,j}^{k} + V_{i-1,j}^{k}}{(\Delta x)^2} + \epsilon_{ij}^{yy} \frac{V_{i,j+1}^{k} + V_{i,j-1}^{k}}{(\Delta y)^2} \right. \\
& + 2\epsilon_{ij}^{xy} \frac{V_{i+1,j+1}^{k} - V_{i+1,j-1}^{k} - V_{i-1,j+1}^{k} + V_{i-1,j-1}^{k}}{4\Delta x \Delta y} \\
& + \left(\frac{\epsilon_{i+1,j}^{xx} - \epsilon_{i-1,j}^{xx}}{2\Delta x} + \frac{\epsilon_{i,j+1}^{yx} - \epsilon_{i,j-1}^{yx}}{2\Delta y} \right) \frac{V_{i+1,j}^{k} - V_{i-1,j}^{k}}{2\Delta x} \\
& \left. + \left(\frac{\epsilon_{i+1,j}^{xy} - \epsilon_{i-1,j}^{xy}}{2\Delta x} + \frac{\epsilon_{i,j+1}^{yy} - \epsilon_{i,j-1}^{yy}}{2\Delta y} \right) \frac{V_{i,j+1}^{k} - V_{i,j-1}^{k}}{2\Delta y} \right\}.
\end{aligned}
\tag{13}
$$

The high-frequency regime

$\epsilon^h_{\parallel}$, $\epsilon^h_{\perp}$: Relative permittivities in the parallel and perpendicular directions for micro- and mm-wave (high-frequency) regime.

$\tan\delta_{\parallel}$, $\tan\delta_{\perp}$: Loss tangents for parallel and perpendicular orientations. Required because the LC material is lossy at these frequencies.

The complex relative permittivities are given by

$$\epsilon^c_{\parallel} = \epsilon^h_{\parallel}(1 - \mathrm{i}\tan\delta_{\parallel}), \quad \epsilon^c_{\perp} = \epsilon^h_{\perp}(1 - \mathrm{i}\tan\delta_{\perp}), \tag{14}$$

with

$$\begin{aligned}
\epsilon^c_{xx} &= \epsilon^c_{\perp} + \Delta\epsilon^c \cos^2\phi(x,y) = \epsilon^h_{xx}(1 - \tan\delta_{xx}), \\
\epsilon^c_{xy} &= \epsilon^c_{yx} = \Delta\epsilon^c \sin\phi(x,y)\cos\phi(x,y) = \epsilon^h_{xy}(1 - \tan\delta_{xy}), \\
\epsilon^c_{yy} &= \epsilon^c_{\perp} + \Delta\epsilon^c \sin^2\phi(x,y) = \epsilon^h_{yy}(1 - \tan\delta_{yy}), \\
\epsilon^c_{zz} &= \epsilon^c_{\perp} = \epsilon^h_{zz}(1 - \tan\delta_{zz}),
\end{aligned} \tag{15}$$

where

$$\begin{aligned}
\epsilon^h_{xx} &= \epsilon^h_{\perp} + \Delta\epsilon^h \cos^2\phi(x,y), \\
\epsilon^h_{xy} &= \epsilon^h_{yx} = \Delta\epsilon^h \sin\phi(x,y)\cos\phi(x,y), \\
\epsilon^h_{yy} &= \epsilon^h_{\perp} + \Delta\epsilon^h \sin^2\phi(x,y), \\
\epsilon^h_{zz} &= \epsilon^h_{\perp}.
\end{aligned}$$

Substituting (14) into (15) and rearranging leads to the following expressions for the $\tan\delta$ values of the tensor entries:

$$\begin{aligned}
\tan\delta_{xx} &= \frac{\epsilon^h_\perp \tan\delta_\perp + (\epsilon^h_\parallel \tan\delta_\parallel - \epsilon^h_\perp \tan\delta_\perp)\cos^2\phi}{\epsilon^h_\perp + \Delta\epsilon^h \cos^2\phi}, \\
\tan\delta_{xy} = \tan\delta_{yx} &= \frac{\epsilon^h_\parallel \tan\delta_\parallel - \epsilon^h_\perp \tan\delta_\perp}{\Delta\epsilon^h}, \qquad (16) \\
\tan\delta_{yy} &= \frac{\epsilon^h_\perp \tan\delta_\perp + (\epsilon^h_\parallel \tan\delta_\parallel - \epsilon^h_\perp \tan\delta_\perp)\sin^2\phi}{\epsilon^h_\perp + \Delta\epsilon^h \sin^2\phi}, \\
\tan\delta_{zz} &= \tan\delta_\perp .
\end{aligned}$$

Electric Potential

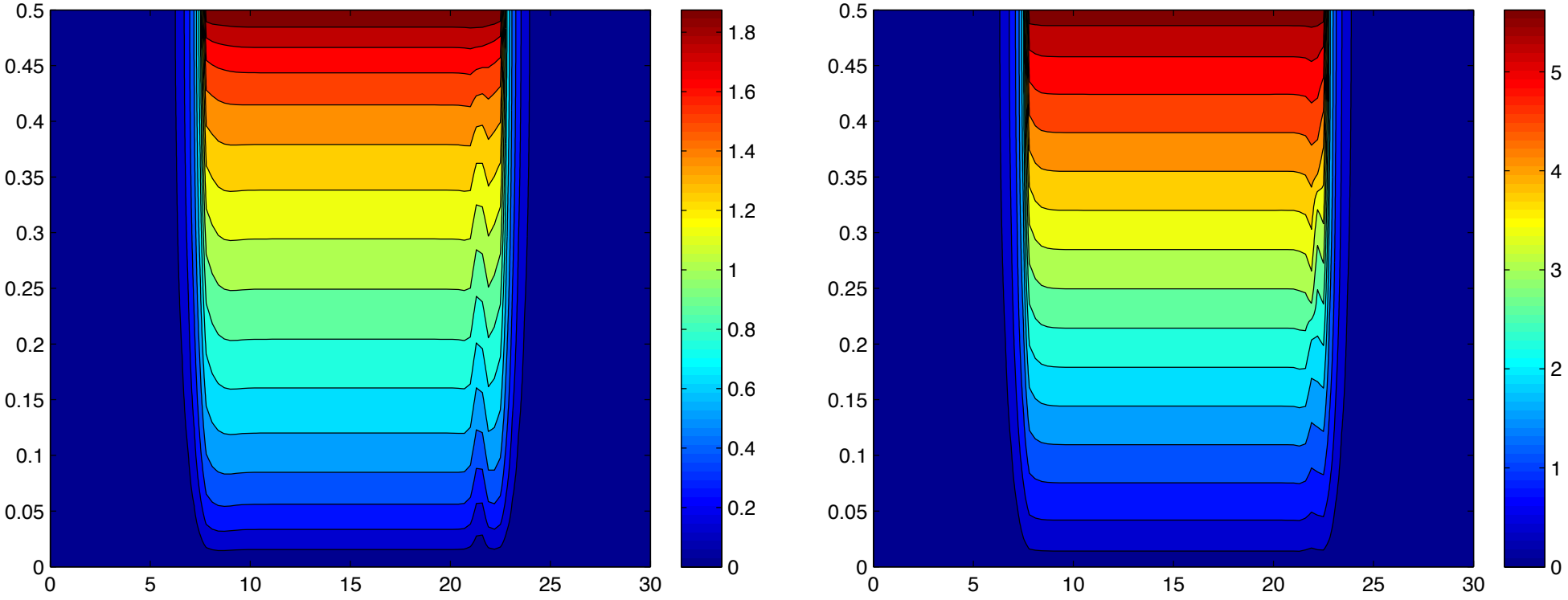

Figure : Electric potential distribution for $V_0 = 2\mathrm{V}$ (left) and $V_0 = 6\mathrm{V}$ (right). Merck E7: $k_{11} = 11.1 \times 10^{-12}$ N, $k_{33} = 17.1 \times 10^{-12}$ N, $\epsilon_{||} = 19$ and $\epsilon_{\perp} = 5.2$.

Director Tilt-Angle

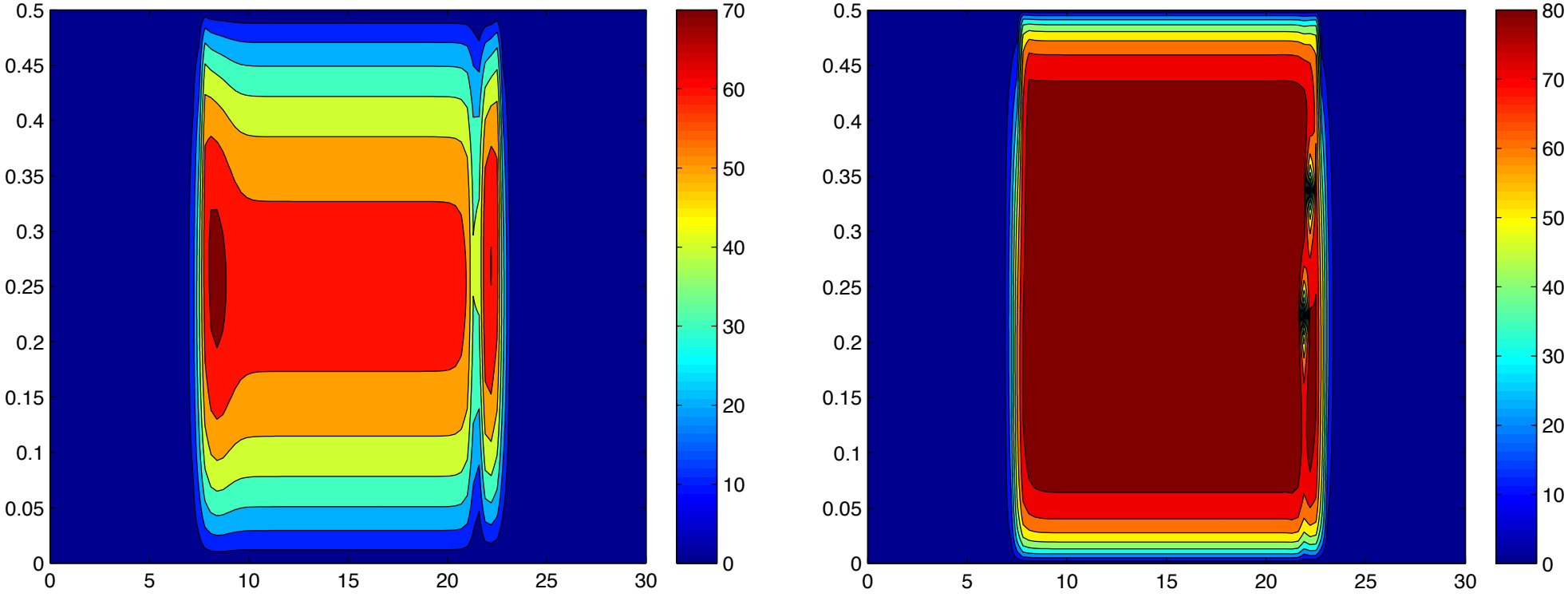

Figure : Director tilt-angle distribution for $V_0 = 2\mathrm{V}$ (left) and $V_0 = 6\mathrm{V}$ (right). Merck E7: $k_{11} = 11.1 \times 10^{-12}$ N, $k_{33} = 17.1 \times 10^{-12}$ N, $\epsilon_{||} = 19$ and $\epsilon_{\perp} = 5.2$.

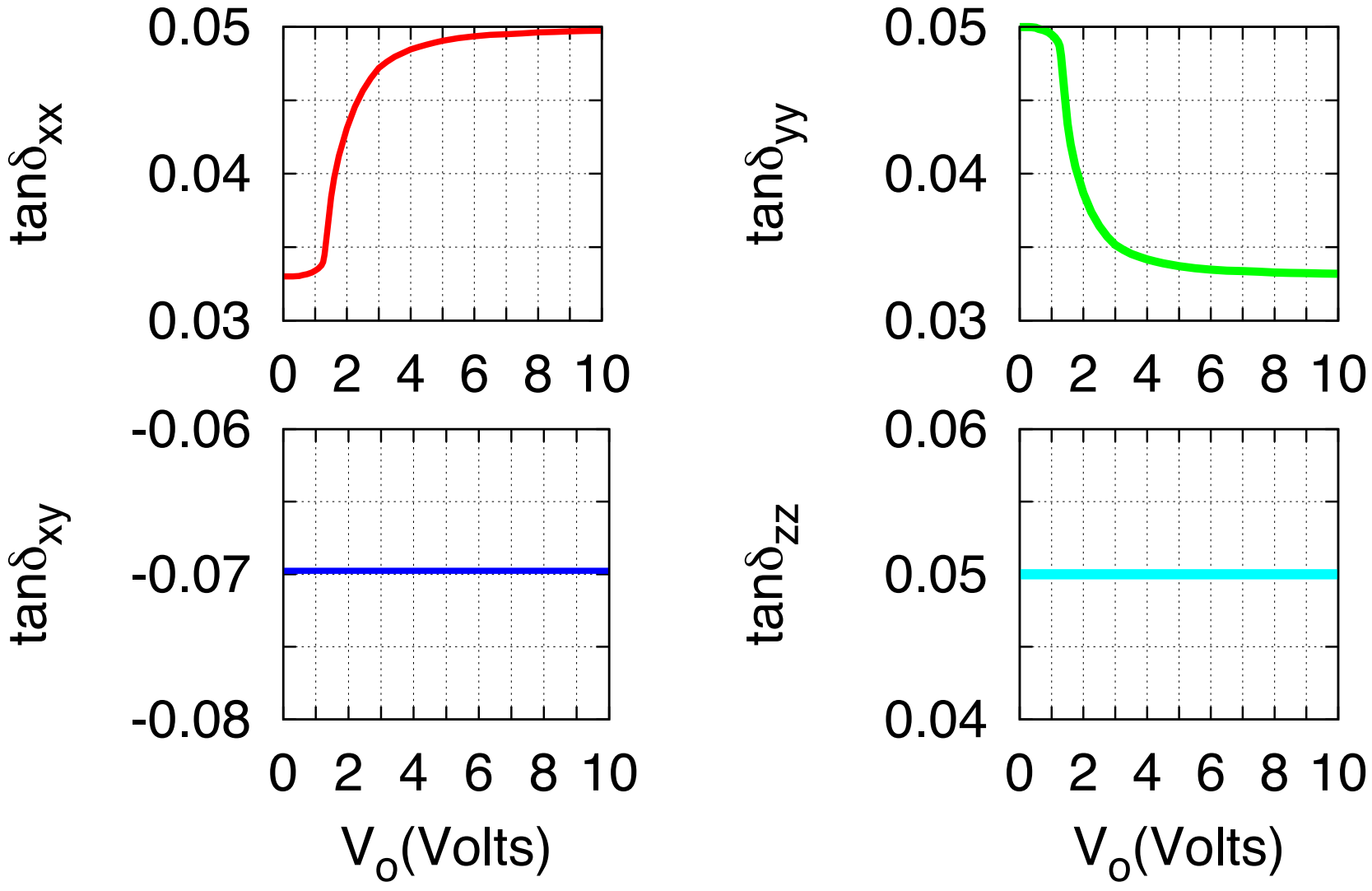

Figure : High-frequency tensor entries of the loss tangent versus bias voltage. $\epsilon_{\|}^{h} = 3.17$, $\epsilon_{\perp}^{h} = 2.72$, $\tan\delta_{\perp} = 0.050$ and $\tan\delta_{\|} = 0.033$, *Bulja et al. 2010* at 30 GHz.

High-frequency tensor entries of the dielectric constant versus bias voltage.

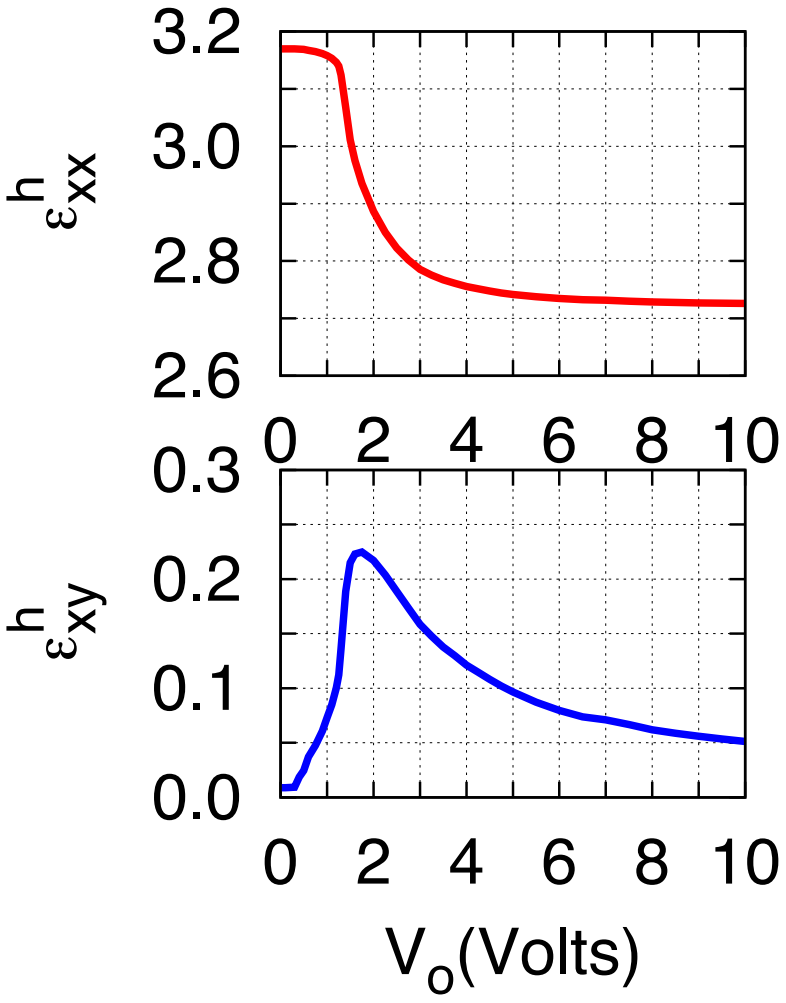

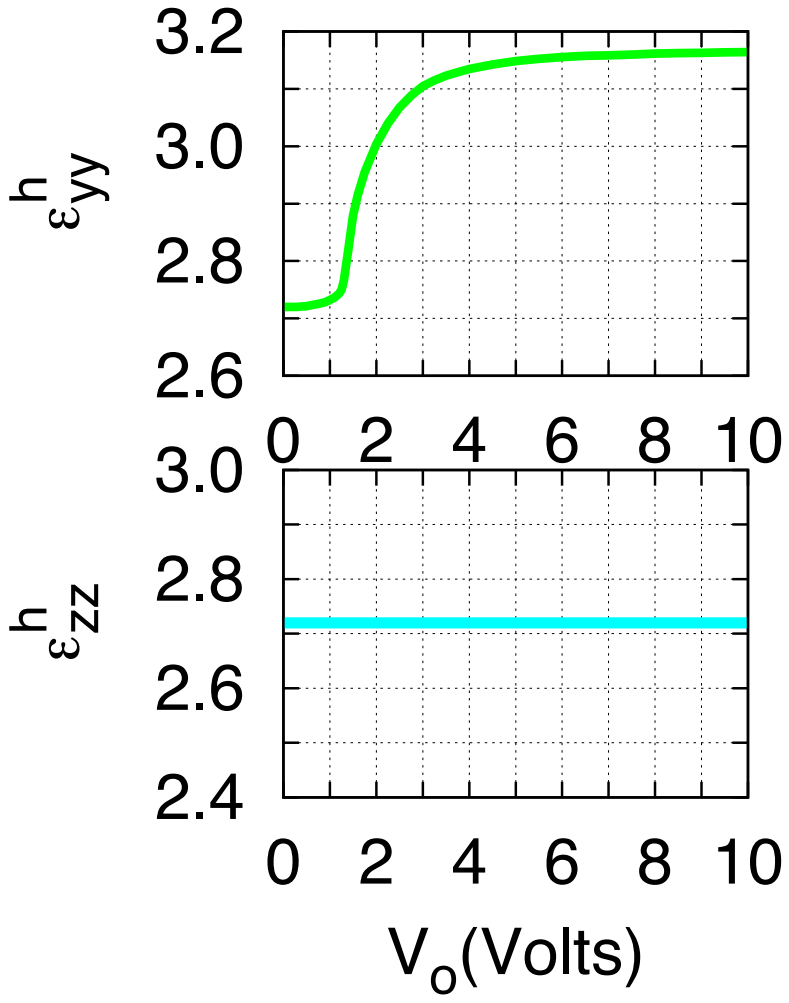

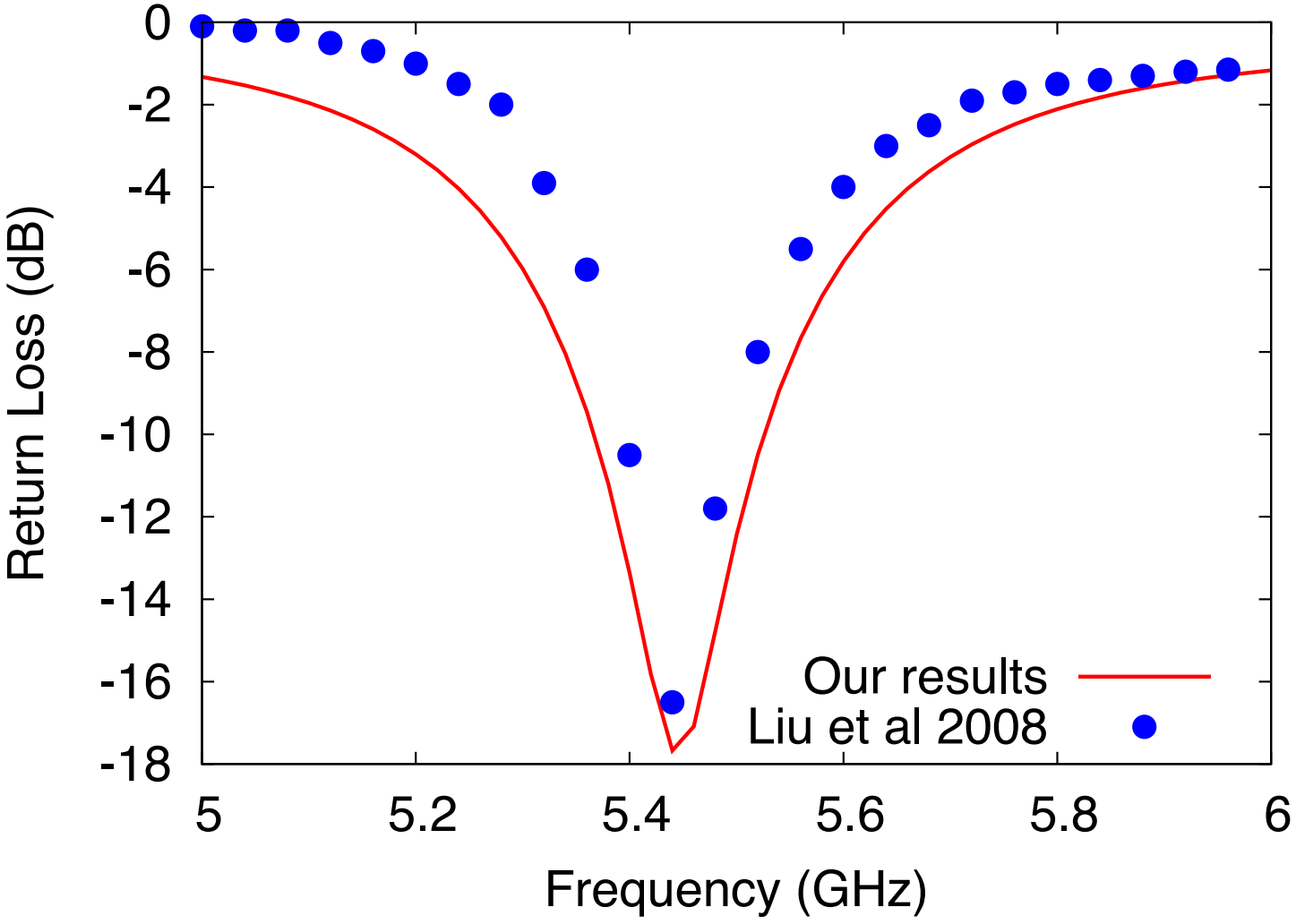

Figure : Comparison with experimental measurements for $V_0 = 10$V. Agreement with our simulations is very good, especially for resonant frequency.

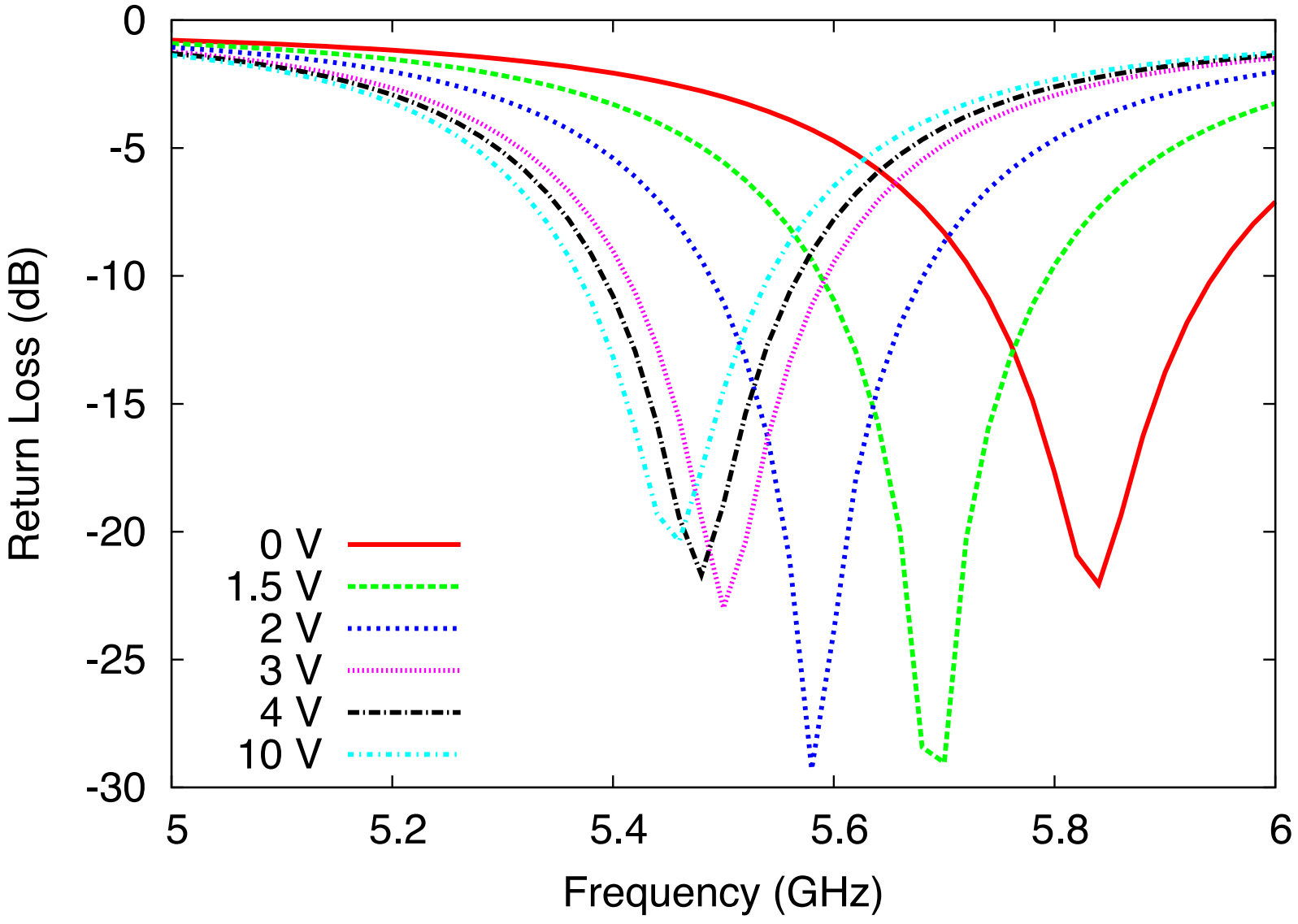

Figure : Tuning the LC-based patch antenna. Return loss Vs frequency for various applied voltages. Note the proximity of the 4 V and 10 V graphs.

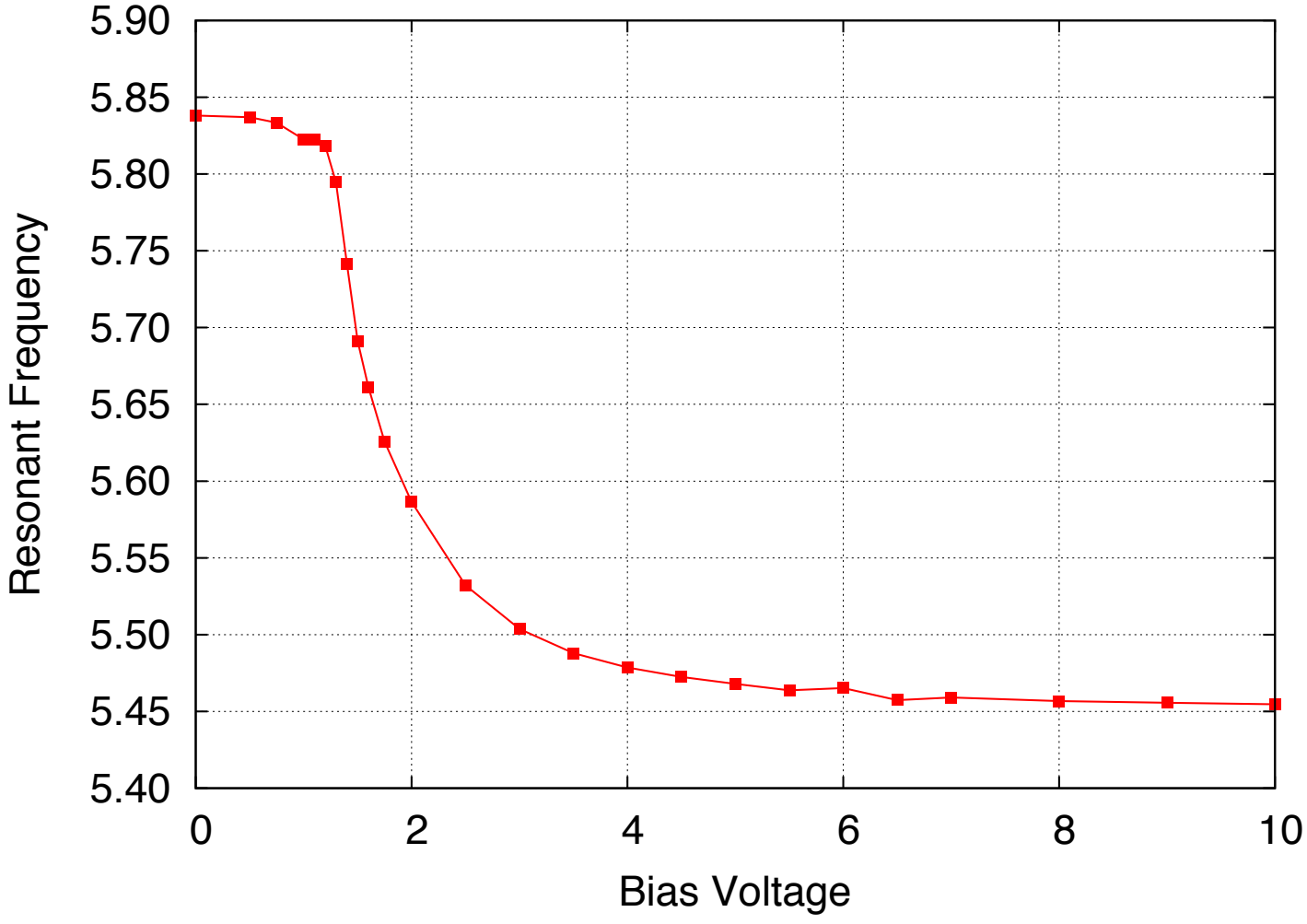

Figure : Resonant Frequency Vs Voltage. Frequency tuning range between 5.45 and 5.82 GHz achieving a return loss less than 20 dB. The antenna can be effectively tuned with a low voltage between 0 and 10 V providing a frequency tuning range of approximately 7%.

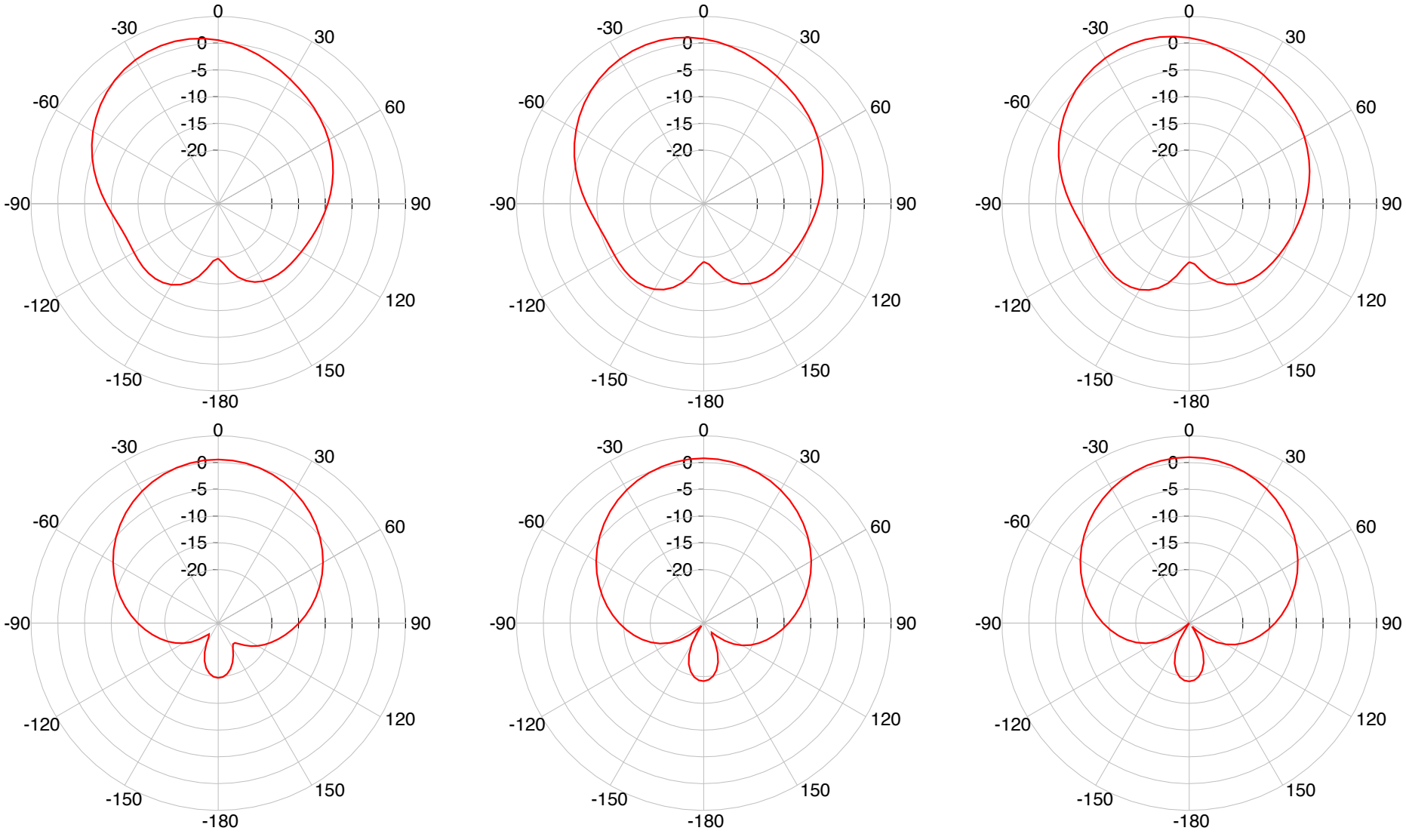

Figure : Realized gain patterns for $V_0 = 0, 2, 4\,V$ (left, center, right) at resonance. Top: yz-plane; Bottom: yx-plane (principle planes).

Summary

- An accurate model for LC-based patch antennas was developed taking into account the dielectric anisotropy and losses of the LC material. The method consisted of:
  (a) Accurately solving the coupled PDE problem obtaining the director field distribution inside the LC.
  (b) Utilizing HFSS to compute the radiation characteristics of the LC-based patch antenna using the material tensors of the LC under different bias fields.
- The simulation results were compared to measurements that appeared in the literature demonstrating good agreement, very good tuning range, and attractive radiation characteristics.
- Liquid crystals are promising materials in microwave engineering with potential applications in antenna technology.
- Additional experimental work must be conducted on the characterization of liquid crystals in the lower microwave frequency range, enabling their widespread use in reconfigurable antenna design and fabrication.

Selected References I

P. de Gennes and J. Prost.
The Physics of Liquid Crystals.
2nd ed, Oxford: Clarendon Press, 1995.

L. Liu and R. J. Langley.
Liquid crystal tunable microstrip patch antenna.
Electr. Lett., 44(20):1179–1180, 2008.

S. Bulja, D. M.-Syahkal, R. James, S. E. Day, and F. A. Fernandez.
Measurements of dielectric properties of nematic liquid crystals at millimeter wavelengths.
IEEE Trans. Microw. Theory Tech., 58(12):3493–3501, December 2010.

R. Bose and A. Sinha.
Tunable patch antenna using a liquid crystal substrate.
Proc. IEEE Rad. Confer., pp. 1–6, 2008

A. C. Polycarpou, M. A. Christou, and N. C. Papanicolaou.
A Mode-Matching Approach to Electromagnetic Wave Propagation in Nematic Liquid Crystals.
IEEE Trans. Microw. Theory Tech., 60(10):2950-2958, October 2012.